BNL-203451-2018-JAAM

# Optimizing the ORR activity of Pd based nanocatalysts by tuning their strain and particle size

W. Xiao, H. L. Xin

To be published in "Journal of Materials Chemistry A"

April 2017

Center for Functional Nanomaterials

**Brookhaven National Laboratory**

**U.S. Department of Energy**

USDOE Office of Science (SC), Basic Energy Sciences (BES) (SC-22)

# DISCLAIMER

# Optimizing the ORR activity of Pd based nanocatalysts by tuning their strain and particle size†

Weiping Xiao,[a] Marco Aurelio Liutheviciene Cordeiro,[b] Mingxing Gong,[a] Lili Han,[c] Jie Wang,[a] Ce Bian,[a] Jing Zhu,[a] Huolin L. Xin[b] and Deli Wang *[a]

Controlling of the particle size and surface strain is the key to tuning the surface chemistry and optimizing the catalytic performance of electrocatalysts. Here, we show that by introducing both Fe and Co into Pd lattices, the surface strain of Pd nanocatalysts can be tuned to optimize their oxygen reduction activity in both fuel cells and Zn–air batteries. The $Pd_2FeCo/C$ alloy particles are uniquely coated with an ultrathin $Fe_2O_3$ shell which is in situ formed during a thermal annealing treatment. The thin shell acts as an effective barrier that prevents the coalescence and ripening of $Pd_2FeCo/C$ nanoparticles. Compared with Pd/C, $Pd_2FeCo/C$ exhibits higher catalytic activity and long-term stability for the ORR, signifying changes in catalytic behavior due to particle sizes and strain effects. Moreover, by spontaneous decoration of Pt on the surface of $Pd_2FeCo/C$, the $Pd_2FeCo$@Pt/C core@shell structure was formed and the Pt mass activity was about 37.6 and 112.5 times higher than that on Pt/C in a 0.1 M $HClO_4$ and KOH solution at 0.9 V, respectively, suggesting an enhanced ORR performance after Pt decoration. More interestingly, $Pd_2FeCo$@Pt/C also shows a power density of ~308 mW $cm^{-2}$, which is much higher than that of Pt/C (175 mW $cm^{-2}$), and excellent durability in a home-made Zn–air battery.

## Introduction

In the search for highly efficient nano-catalysts toward the oxygen reduction reaction (ORR), an important cathodic reaction in low-temperature polymer electrolyte membrane fuel cells and metal–air batteries, relatively low-cost Pd-based nanocatalysts have attracted great interest.[1–8] Recent studies have revealed that the addition of an early transition metal to Pd can cause Pd–Pd bond compression, resulting in d-band center down-shift and changes in the electronic structure of Pd.[9–12] Due to these structural changes, the adsorption of OH is mostly centered on the second metal and the Pd–O binding strength is optimized to the level where Pd catalysis of the ORR may become comparable to that of Pt.[13,14] In general, this structural transformation requires high temperature annealing (>500 °C), which inevitably leads to the aggregation of the nanoparticles and then decreases the mass activity.[15,16]

Hence, tremendous efforts had been concentrated to prevent the coalescence and reduce the particle size during annealing for catalyst design and optimization.[17,18] One of the efficient strategies is to employ protective coatings on the surface including carbon shells,[19,20] oxide shells,[16,21,22] inorganic barriers,[23–25] graphitic hollow spheres,[26,27] etc. However, it was criticized that the presence of a protective layer can decrease the catalytic performance by blocking the active sites and lowering the mass transport rate to some extent. Hence, additional steps to remove the coating layer are required to expose the active sites, which are time consuming and cost intensive processes.[16] Therefore, exploring a convenient and feasible protective coating strategy to prevent the agglomeration of nanoparticles without affecting their electrocatalytic performance is desirable.

Herein, we report highly durable and active $Pd_2FeCo/C$ nanoparticles featuring an ultrathin $Fe_2O_3$ shell. This shell was spontaneously formed during thermal annealing to obtain a structure with a high alloying degree. The $Fe_2O_3$ shell effectively prevents the $Pd_2FeCo/C$ nanoparticles from coalescence during the annealing treatment so that the $Pd_2FeCo/C$ nanoparticles were as small as 6.5 nm. Moreover, the $Fe_2O_3$ shell was so thin (1.1 nm) that it could be readily dissolved during the electrochemical activation process before ORR performance testing, and the $Pd_2FeCo/C$ nanoparticles exhibited comparable ORR electrocatalytic activity to Pt/C. To further enhance the

[a]Key Laboratory of Material Chemistry for Energy Conversion and Storage (Huazhong University of Science and Technology), Ministry of Education, Hubei Key Laboratory of Material Chemistry and Service Failure, School of Chemistry and Chemical Engineering, Huazhong University of Science and Technology, Wuhan, 430074, P. R. China. E-mail: wangdl81125@hust.edu.cn

[b]Center for Functional Nanomaterials, Brookhaven National Laboratory, Upton, NY, USA

[c]School of Materials Science and Engineering Tianjin University, No. 92, Weijin Road, Nankai District, Tianjin, P. R. China

† Electronic supplementary information (ESI) available. See DOI: 10.1039/c7ta02479g

ORR performance, by a spontaneous replacement reaction, $Pd_2FeCo$@Pt/C is successfully synthesized and exhibits super-high electrocatalytic performance toward the ORR in both 0.1 M $HClO_4$ and 0.1 M KOH, which can be attributed to the high active core and ultrathin Pt shell. More interestingly, when assembled in a home-made Zn–air battery device, $Pd_2FeCo$@Pt/C also shows excellent electrochemical performance.

# Experimental

## Material synthesis

$Pd_2FeCo$/C nanoparticles are prepared by a simple method as previously reported.[28] In detail, $PdCl_2$, $CoCl_2$, $FeCl_3$ and the Vulcan XC-72 carbon support were mixed into 10 mL water to obtain 20 wt% Pd. The mixture slurry was obtained by the evaporation of water and then reduced with $H_2$ at 300 °C. Thermal annealing of carbon-supported $Pd_2FeCo$/C nanoparticles at 500 °C for 10 h under a $N_2$ atmosphere leads to the formation of nanoparticles with a high alloying degree with the $Fe_2O_3$ thin layer coating. PdCo/C and PdFe/C catalysts were synthesized by the same method. For comparison, Pd/C and Pt/C catalysts with a weight ratio of 20% are synthesized via the same procedure at a heating temperature of 150 °C for 2 h under a $H_2$/Ar atmosphere.

The $Pd_2FeCo$@Pt/C catalyst was prepared by the replacement of Pd, Co, and Fe with Pt. Briefly, the synthesized $Pd_2FeCo$/C and $K_2PtCl_4$ with a mole ratio of 30 : 1 were suspended in an aqueous solution, which is calculated to be about one monolayer of Pt on $Pd_2FeCo$/C nanoparticles. The mixed solution was heated at 60 °C under magnetic stirring and then the solid product was recovered by centrifugation and dried at 60 °C overnight.

## Materials characterization

X-ray diffraction (XRD) of the synthesized catalysts was performed by using an X'Pert PRO diffractometer in the scan range from 15° to 85° at a scan rate of 4° $min^{-1}$. Scanning transmission electron microscopy (STEM) and energy-dispersive X-ray spectroscopy (EDX) measurements were performed on an FEI Talos F200X operated at 200 keV. TEM samples were prepared by drop casting the particle dispersions on carbon-coated Cu grids and drying under ambient conditions. X-ray photoelectron spectroscopy (XPS) was performed on AXIS-ULTRA DLD-600W equipment. ICP-AES was investigated by using an IRIS Advantage (Thermo Elemental Co., USA).

## Electrochemical testing

Electrochemical measurements were conducted in 0.1 M $HClO_4$ or 0.1 M KOH solution. The catalyst applied to a glassy carbon (GC) disk, a Pt wire and a reversible hydrogen electrode (RHE) were used as a working electrode, the counter electrode and the reference electrode, respectively. CVs and CO stripping curves were measured in nitrogen-saturated 0.1 M $HClO_4$ at a scan rate of 50 mV $s^{-1}$. The electrochemically active surface area (ECSA) was obtained from the current density of hydrogen in the potential deposition region (0.05–0.4 V). ORR evaluation was conducted in $O_2$-saturated 0.1 M $HClO_4$ and 0.1 M KOH solutions, at a scan rate of 5 mV $s^{-1}$ and a rotation rate of 1600 rpm. The durability test was conducted in $O_2$-saturated 0.1 M $HClO_4$ and 0.1 M KOH solutions in the potential range between 0.6 and 1.0 V, at a scan rate of 100 mV $s^{-1}$.

For the Zn–air battery performance test, 6 M KOH + 0.2 M $Zn(CH_3COO)_2$ and polished Zn foil were used as the electrolyte and anode electrode, respectively. $Pd_2FeCo$@Pt/C served as the catalyst for the ORR. The mass loading was 0.5 mg $cm^{-2}$. A LAND-CT2001A testing device was used to carry out the cycling test at 5 mA $cm^{-2}$ and 20 mA $cm^{-2}$.

# Results and discussion

The X-ray diffraction (XRD) patterns of the Pd-based nanoparticles were collected to characterize the structural changes. As shown in Fig. 1a, the as-synthesized Pd/C, PdFe/C, PdCo/C and $Pd_2FeCo$/C show the typical four diffraction peaks corresponding to the (111), (200), (220), and (311) planes of the face centered cubic (fcc) Pd phase, respectively. The peak positions of PdFe/C, PdCo/C and $Pd_2FeCo$/C shifted to higher angles relative to Pd/C, indicating that the smaller atoms Fe and Co entered the Pd lattice. Based on the XRD patterns and Debye–Scherrer equation[29] (Table 1), the lattice contraction of the PdCo/C nanoparticles (4.09%) is higher than that of PdFe/C (0.57%), indicating that it is easier for the Co atom to enter the Pd lattice than for the Fe atom. For PdFe/C nanoparticles, the replacement of Fe with Co to form $Pd_2FeCo$/C can improve the alloying degree. Hence, the lattice contraction of the $Pd_2FeCo$/C nanoparticles (2.24%) is smaller than that of PdCo/C and higher than that of PdFe/C. The lattice contraction reflects a decrease in the Pd surface adsorption strength for the oxygen-containing species ($O_{ads}$) and an increase in the catalytic performance

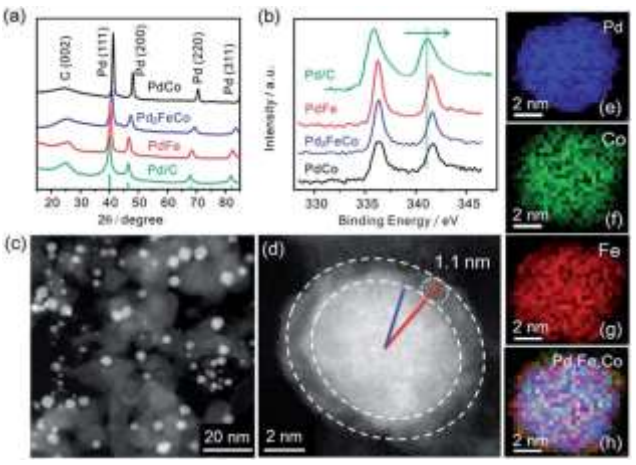


Fig. 1 (a) XRD patterns of Pd/C, PdFe/C, PdCo/C and $Pd_2FeCo$/C. The vertical green line corresponds to the peak positions of pure Pd (PDF card # 01-089-4897). (b) Pd 3d fine XPS spectra of Pd/C, PdFe/C, PdCo/C and $Pd_2FeCo$/C. (c) Overview Z-contrast STEM image of $Pd_2FeCo$/C. (d) Z-contrast STEM image of a single $Pd_2FeCo$/C nanoparticle. The dark-contrast patches (highlighted by the dotted line) show the absence of Co and Pd. STEM-EDX elemental maps of Pd (e), Co (f), Fe (g) and the composite (h) from a $Pd_2FeCo$/C nanoparticle.

Table 1 XRD results of different catalysts

| Catalyst | 2θ/degree (220) | Lattice parameter (nm) | Crystallite size (nm) | Strain (%) |
|---|---|---|---|---|
| Pd/C | 68.11 | 0.3889 | 12.7 | — |
| PdFe/C | 68.49 | 0.3867 | 10.5 | 0.57 |
| PdCo/C | 70.85 | 0.3730 | 15.4 | 4.09 |
| $Pd_2FeCo/C$ | 69.57 | 0.3802 | 8.48 | 2.24 |

toward the ORR.[30,31] According to Table 1, the particle size of $Pd_2FeCo/C$ nanoparticles is smaller than those of PdFe/C and PdCo/C nanoparticles, indicating more active sites on the $Pd_2$-FeCo/C surface. In addition, the electronic structure of Pd would be changed by adding Co and Fe atoms, which was verified by the X-ray photoelectron spectroscopy (XPS) spectra in Fig. 1b. It can be seen that the binding energy of Pd 3d in PdFe/C, PdCo/C and $Pd_2FeCo/C$ exhibits a 0.75 eV, 0.88 eV, and 0.85 eV shift to higher binding energies compared with that of Pd/C. The shifting of binding energy leads to a downward shift in the Pd d-band center and then weakening of the $O_{ads}$ adsorption strength, resulting in the enhancement of ORR electrocatalytic activity.[30,31]

Scanning transmission electron microscopy (STEM) in conjunction with energy-dispersive X-ray spectroscopy (EDX) is used to characterize the structure and chemical composition of the nanoparticles. The $Pd_2FeCo/C$ nanoparticles featuring an ultrathin $Fe_2O_3$ shell can be seen from Fig. 1c–h and S1.† The $Fe_2O_3$ shell is spontaneously formed during the thermal annealing of $Pd_2FeCo/C$ nanoparticles to obtain a high alloying degree. The $Fe_2O_3$ shell adjacent to the $Pd_2FeCo/C$ nanoparticles was further certified by TEM and the thickness of the shell was as thin as 1.1 nm (Fig. 1d and S1†). The $Fe_2O_3$ shell effectively prevents the $Pd_2FeCo/C$ nanoparticles from coalescence during the annealing treatment so that the $Pd_2FeCo/C$ nanoparticles were as small as 6.5 nm (Fig. 1c), which was smaller than that of PdFe/C (Fig. S2†) and PdCo/C (Fig. S3†) and close to the particle size calculated from XRD measurement. Furthermore, the atomic-scale chemical maps, as can be seen in Fig. 1e–h, clearly showed an Fe-rich shell, which is in agreement with the XPS result that Fe is rich on the surface of the particles (Fig. S4†).

The electrocatalytic properties of the prepared nanoparticles for the ORR are investigated by using a rotating disk electrode. The ORR polarization curves of different catalysts are exhibited in Fig. 2a. The half-wave potential ($E_{1/2}$) on the $Pd_2FeCo/C$ catalyst was +0.860 V, comparable to Pt/C (+0.861 V), which showed a 77 mV positive shift relative to the Pd/C catalyst. The electron transfer number on the $Pd_2FeCo/C$ nanoparticles was calculated to be 4.0 from the Koutecky–Levich (K–L) equation (Fig. S5†). Furthermore, the mass activity (MA) and specific activity (SA) of $Pd_2FeCo/C$ at 0.85 V are more than 2.92 and 2.66 times higher than those of PdFe/C, 2.62 and 1.83 times higher than those of PdCo/C and 9.08 and 10.64 times higher than those of Pd/C (Fig. S6†). On the one hand, the enhanced ORR catalytic performance on $Pd_2FeCo/C$ can be attributed to the small particle size (Table 1), which is consistent with the result

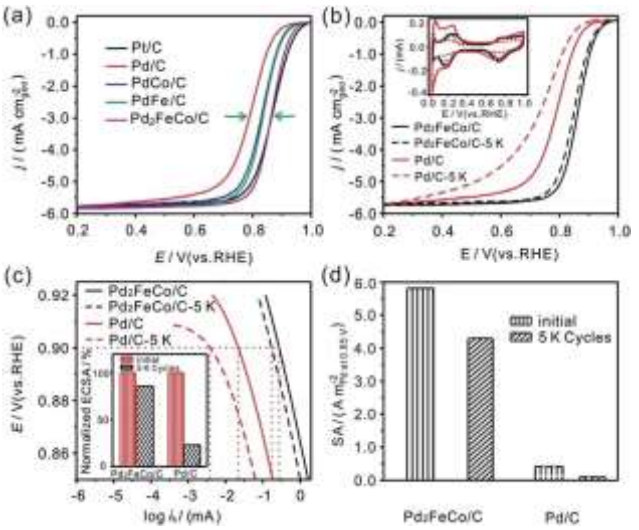


Fig. 2 (a) ORR polarization curves of Pd/C, PdFe/C, PdCo/C, $Pd_2$-FeCo/C and Pt/C. (b) ORR polarization curves of $Pd_2FeCo/C$ and Pd/C before and after 5000 potential cycles. The inset shows the changes in the CV profiles during 5000 potential cycles. (c) Comparison of dynamic current ($i_k$). The inset shows the changes of the ECSA from the CV profiles. (d) SA comparison on $Pd_2FeCo/C$ and Pd/C electrodes at 0.85 V before and after 5000 potential cycles.

from cyclic voltammetry (CV) curves (Fig. S7 and S8†). $Pd_2FeCo/C$ nanoparticles show a larger hydrogen area and ECSA compared with PdCo/C and PdFe/C, indicating more desirable surface active sites on $Pd_2FeCo/C$. On the other hand, the enhanced ORR catalytic performance on $Pd_2FeCo/C$ is probably attributed to the lattice-strain and electronic effects. As can be seen in Fig. S9,† there is a volcano-curve relationship between the lattice parameter, the binding energy of the Pd-based catalysts and the specific activity. With increasing alloying degree, the lattice contraction and d-band center downward shift may cause a weaker Pd–O adsorption and an improvement in the electrocatalytic performance toward the ORR, while the surface-ligand effect resulted in a decrease in electrocatalytic performance. The two opposite effects lead to the observed "volcano curve" relationship. Moreover, the ORR performance of $Pd_2$-FeCo/C-300 is compared with that of $Pd_2FeCo/C$-500 nanoparticles as shown in Fig. S10.† The ORR kinetics were dramatically accelerated on $Pd_2FeCo/C$-500 nanoparticles and the half-wave potential ($E_{1/2}$) was significantly shifted toward a positive potential relative to that of $Pd_2FeCo/C$-300, indicating a significant increase of the ORR activity. The enhanced ORR activity could be attributed to the electronic effect. $Pd_2FeCo/C$-500 nanoparticles had a higher lattice contraction and alloying degree relative to $Pd_2FeCo/C$-300 (Fig. S11†), which would cause a weaker Pd–O adsorption and an improvement in the electrocatalytic performance for the ORR.

The CV and ORR curves of $Pd_2FeCo/C$ and Pd/C catalysts before and after the 5000 cycle durability test are shown in Fig. 2b. It can be seen that the $Pd_2FeCo/C$ nanoparticles exhibit superior long-term stability with negligible activity loss compared with Pd/C. According to the CV curve comparison, Pd/C shows significant decrease (77.4%) in the ECSA after the

durability test. However, there is only 14.4% decrease in the ECSA of $Pd_2FeCo/C$, indicating a small loss of the electrochemically active surface area (inset of Fig. 2b and c). Furthermore, the decrease of the specific activity on the $Pd_2FeCo/C$ catalyst was much smaller than that on Pd/C (Fig. 2d). Based on the above analysis, it is clear that the alloyed $Pd_2FeCo/C$ exhibits superior ORR activity and stability relative to Pd/C probably due to the lattice-strain effect.

To further improve the activity and stability of the $Pd_2FeCo/C$ nanoparticles for practical application, $Pd_2FeCo@Pt/C$ catalysts were prepared via a simple method. The TEM image in Fig. 3a shows that the $Pd_2FeCo@Pt/C$ nanoparticles were dispersed well on the carbon support and the particle size was calculated to be about 6.2 nm, which is close to the initial size of the $Pd_2FeCo/C$ nanoparticles (6.5 nm). The lattice spacing was measured to be 0.222 nm, corresponding to the Pd (111) crystal surface (inset in Fig. 3a). To directly measure the surface and subsurface chemical composition with atomic-scale resolution, STEM-EDX elemental maps were used to investigate a single particle. The Fe rich shell on $Pd_2FeCo/C$ nanoparticles (Fig. 1d and h) disappeared after Pt decoration, which can be clearly seen from the HRTEM image (inset in Fig. 3a) and the composite maps of Co and Fe (Fig. 3h). Furthermore, a Pt rich shell can be seen from the composite maps of Pt, Pd, Co and Fe (Fig. 3d–i), which indicates the successful decoration of Pt on $Pd_2FeCo/C$ nanoparticles, and is consistent with the ideal atomic arrangement (Fig. 3b). Moreover, from the quantitative analysis using inductively coupled plasma mass spectrometry (ICP-AES) (Table S1†), the atomic ratio of Pd and Pt was measured to be 66.7 : 1, which was close to the nominal ratio of 60 : 1.

The ORR electrocatalytic performance of $Pd_2FeCo@Pt/C$ nanoparticles was compared with those of $Pd_2FeCo/C$, Pd/C and Pt/C catalysts. The CV and CO stripping curves of $Pd_2FeCo/C$ nanoparticles with and without Pt decoration in Fig. 4a and b indicated that $Pd_2FeCo@Pt/C$ nanoparticles exhibit positive potential shift for surface oxide reduction and negative potential shift for CO stripping, which confirmed that Pt had been

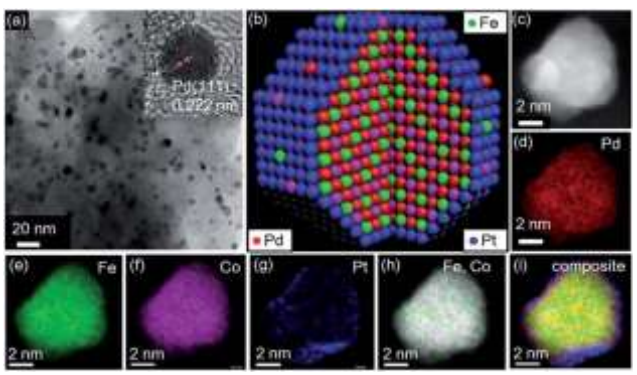


Fig. 3 (a) TEM image of $Pd_2FeCo@Pt/C$ nanoparticles; the inset shows the HRTEM image of one particle. (b) The simulated crystal structures of $Pd_2FeCo@Pt/C$. (c) STEM image of one particle. STEM-EDX elemental maps of Pd (d), Fe (e), Co (f), Pt (g), and the composites of Fe and Co (h) and Fe, Co, Pd, and Pt (i).

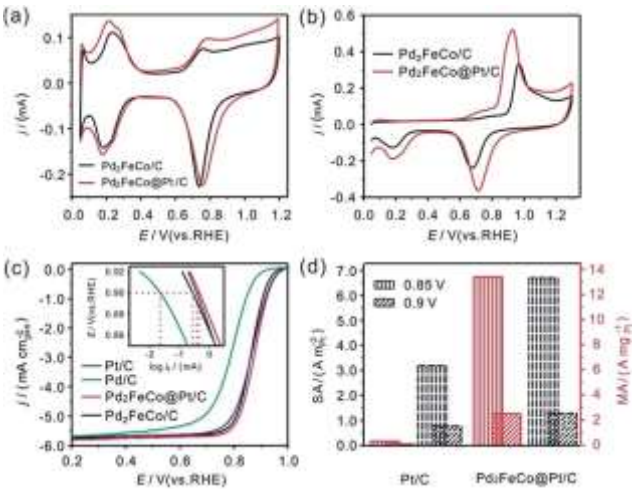


Fig. 4 (a) CV and (b) CO stripping curves of $Pd_2FeCo/C$ with and without Pt decoration in $N_2$-saturated 0.1 M $HClO_4$ solution. (c) ORR polarization curves of different catalysts in $O_2$-saturated 0.1 M $HClO_4$ solution. The inset shows the comparison of dynamic current ($i_k$). (d) MA and SA comparison on Pt/C and $Pd_2FeCo@Pt/C$ catalysts normalized to the ECSA and Pt loading.

successfully decorated on the surface of $Pd_2FeCo/C$. The ORR polarization curves in Fig. 4c indicate that the half-wave potential of $Pd_2FeCo@Pt/C$ is 0.880 V, which is positively shifted about 19 mV relative to $Pd_2FeCo/C$ and Pt/C, suggesting excellent ORR activity. The electron transfer number (n) on $Pd_2FeCo@Pt/C$ nanoparticles was calculated to be 4.0, indicating the reduction of $O_2$ to $H_2O$ (Fig. S12†). The SA and MA of $Pd_2FeCo@Pt/C$ for the ORR at 0.9 V were calculated to be 1.28 A $m^{-2}$ and 2.5 A $mg_{Pt}^{-1}$, which are 1.73 and 37.6 times higher than those of the Pt/C tested under the same conditions, respectively (Fig. 4d).

After the 10 000 cycle durability test, the CV curves of the $Pd_2FeCo@Pt/C$ electrode decreased slightly and the $E_{1/2}$ negatively shifted about 13 mV after 10 000 cycles (Fig. 5a and S13†), which is much smaller than that of the $Pd_2FeCo/C$ electrode (21 mV, 5000 cycles). In contrast, the CV curve and $E_{1/2}$ of Pt/C

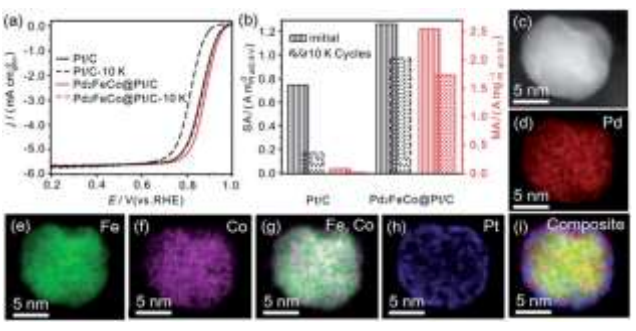


Fig. 5 (a) ORR polarization curves of Pt/C and $Pd_2FeCo@Pt/C$ before and after 10 000 potential cycles in $O_2$-saturated 0.1 M $HClO_4$. (b) MA and SA comparison on Pt/C and $Pd_2FeCo@Pt/C$ before and after 10 000 cycles. (c) Z-contrast STEM image of $Pd_2FeCo@Pt/C$. STEM-EDX elemental maps of Pd (d), Fe (e), Co (f), Fe vs. Co (g), Pt (h) and the composites of Pd, Fe, Co and Pt (i) after 10 000 cycles.

suffered large decrease with about 52 mV decay after 10 000 cycles (Fig. 5a and S13†). Fig. 5b compares the MA and SA changes during the durability test. The data clearly reveal that $Pd_2FeCo$@Pt/C shows much higher performance and very little attenuation compared with pure Pt/C. The enhanced activity and durability could be attributed to the ultrathin Pt shell. To directly visualize the effect of Pt shell, Z-contrast STEM and STEM-EDX elemental mappings were performed on the $Pd_2$-FeCo@Pt/C catalyst after 10 000 cycles (Fig. 5c–i). The Pt rich shell can be seen from the composite maps of Co, Fe, Pt and Pd after 10 000 cycles, signifying that the surface Fe and Co were dissolved after 10 000 cycles. Furthermore, ICP-AES measurements on the $Pd_2FeCo$@Pt/C catalyst after the durability test were conducted and the results can be seen in Table S1.† The atomic ratio of Pd : Fe : Co after electrochemical measurements is larger than the result obtained before the durability test, which indicated that the surface Fe and Co were dissolved after 10 000 cycles. These results demonstrate that ultra-low loading of the Pt shell prevents the dissolution of the $Pd_2FeCo$/C core and further enhances the stability of the catalyst.

As mentioned above, the prepared $Pd_2FeCo$@Pt/C nanoparticles exhibited super high ORR activity and durability in 0.1 M $HClO_4$ solution. In addition, the ORR performance in alkaline media plays an important role in Zn–air batteries. Fig. 6a shows the polarization curve comparison of $Pd_2FeCo$@Pt/C, Pt/C and Pd/C for the ORR in 0.1 M KOH solution. The data clearly reveal that $Pd_2FeCo$@Pt/C nanoparticles exhibit the highest performance followed by Pd/C and Pt/C in terms of the half-wave potential, and the Pt mass activity is about 5.4 A $mg_{Pt}^{-1}$, which is 112.5 times higher than that on Pt/C at 0.9 V. The electron transfer number was calculated to be 4.0 for the $Pd_2$-FeCo/C catalyst from the K–L equation (inset of Fig. 6a). In order to investigate the durability of the high performance $Pd_2$-FeCo@Pt/C catalyst, a 30 000 potential cycle durability test was conducted. As can be seen from Fig. 6b, $Pd_2FeCo$@Pt/C nanoparticles showed excellent durability performance, only about 5 mV negatively shifted on half-wave potential after the durability test. Furthermore, after 30 000 cycles, the Pt mass activity on the $Pd_2FeCo$@Pt/C catalyst at 0.9 V was about 3.6 A $mg_{Pt}^{-1}$, which is still much higher than that of Pt/C (0.048 A $mg_{Pt}^{-1}$) (inset of Fig. 6b). The Pt mass activity at 0.9 V of previously reported state-of-the-art materials with a PdM (AuM) core and Pt (PtM) shell is listed in Table S2.† Compared with the materials listed in the literature, the Pt mass activity of the as-prepared $Pd_2$-FeCo@Pt/C nanoparticles is well beyond the DOE 2017 target (0.44 A $mg_{Pt}^{-1}$@0.9 V) and that of most reported materials. The excellent ORR performance on $Pd_2FeCo$@Pt/C nanoparticles can be attributed to the highly active core and the ultrathin Pt shell.

Based on the superior ORR performance of $Pd_2FeCo$@Pt/C in alkaline solution presented above, the zinc–air battery performance was tested by using zinc foil as the anode and $Pd_2$-FeCo@Pt/C nanoparticles loaded on a gas-diffusion electrode as the air electrode. As shown in Fig. 6c, the $Pd_2FeCo$@Pt/C catalyst delivered a much higher current density (365 mA $cm^{-2}$) and peak power density (308 mW $cm^{-2}$) than those on Pt/C and $Pd_2FeCo$/C. More importantly, compared with the previously reported catalysts (Table S3†), the prepared $Pd_2FeCo$@Pt/C catalyst shows a relatively higher peak power density, which corresponds to the excellent ORR performance. Normalized to the mass of consumed Zn during the long-term galvanostatic discharge process, the specific capacity of the battery with $Pd_2FeCo$@Pt/C as the catalyst was over 765 mA h $g_{Zn}^{-1}$ (5 mA $cm^{-2}$) and 650 mA h $g_{Zn}^{-1}$ (20 mA $cm^{-2}$), which is equivalent to ~93.2% and ~79.3% of the theoretical capacity (~820 mA h $g_{Zn}^{-1}$) (Fig. S14†). Furthermore, by replacement of the Zn plate, the battery can continuously discharge for over 100 h with only 38 mV potential loss, indicating the excellent catalytic stability toward the ORR. These results clearly reveal that the developed $Pd_2FeCo$@Pt/C catalyst is a highly competitive alternative to commercial Pt/C for the ORR and could be utilized for other electrochemical devices such as metal–air batteries and fuel cells.

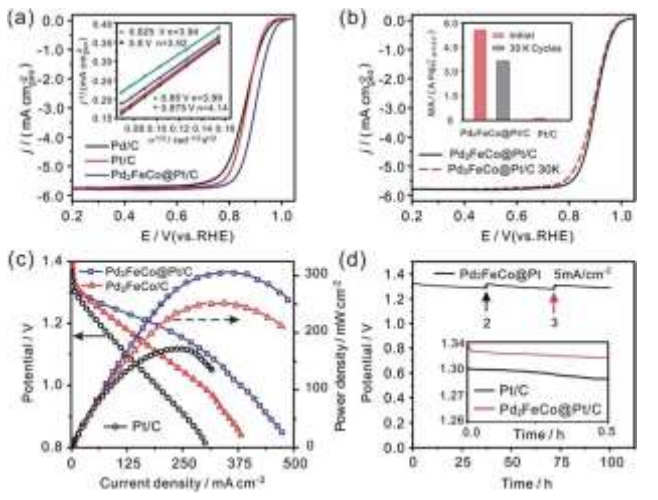


Fig. 6 (a) ORR curve comparison of Pd/C, $Pd_2FeCo$@Pt/C and Pt/C in $O_2$-saturated 0.1 M KOH solution. The inset shows the Koutecky–Levich plots on $Pd_2FeCo$@Pt/C at different potentials. (b) ORR curves of the $Pd_2FeCo$@Pt/C catalyst before and after 30 000 potential cycles. The inset shows the MA comparison of Pt/C and $Pd_2FeCo$@Pt/C nanoparticles at 0.9 V before and after 30 000 cycles. (c) Polarization and power density curves of Zn–air batteries using Pt/C, $Pd_2FeCo$/C and $Pd_2FeCo$@Pt/C nanoparticles at a scan rate of 5 mV $s^{-1}$. (d) Long-term durability of the Zn–air battery using $Pd_2FeCo$@Pt/C as the cathode catalyst at a current density of 5 mA $cm^{-2}$. The inset shows the discharge curves of the Zn–air batteries using Pt/C and $Pd_2$-FeCo@Pt/C as the ORR catalyst.

## Conclusions

In summary, the nanoparticle size of Pd-based catalysts was decreased by controlling the $Pd_2FeCo$/C structure with a spontaneously formed thin layer $Fe_2O_3$ shell which prevents the coalescence of the nanoparticles during the thermal annealing process. The present work offers concrete evidence that surface strain in alloyed nanoparticles can be readily tuned by adding Co and Fe elements to achieve optimal electrocatalytic performance. Moreover, an ultralow amount of Pt has been successfully decorated on $Pd_2FeCo$/C nanoparticles forming a $Pd_2FeCo$@Pt/C core–shell structure, which exhibits much higher ORR

electrocatalytic activity and long-term stability and excellent Zn–air battery performance. The enhanced activity and stability were attributed to a compressive strain effect and smaller particle sizes. The strategy provides a method to rationally tune the catalytic performance for many other chemical reactions.

## Acknowledgements

This work was supported by the National Natural Science Foundation (21573083), the 1000 Young Talent program (grant to Deli Wang), and the Program for New Century Excellent Talents in Universities of China (NCET-13-0237). We thank the Analytical and Testing Center of Huazhong University of Science & Technology for allowing us to use its facilities. S/TEM work was carried out at the Center for Functional Nanomaterials, Brookhaven National Laboratory, which is supported by the U.S. Department of Energy, and the Office of Basic Energy Sciences, under Contract No. DE-SC0012704.

## Notes and references

1 Y. Li, W. Zhou, H. Wang, L. Xie, Y. Liang, F. Wei, J. C. Idrobo, S. J. Pennycook and H. Dai, Nat. Nanotechnol., 2012, **7**, 394–400.

2 X. Huang, Z. Zhao, L. Cao, Y. Chen, E. Zhu, Z. Lin, M. Li, A. Yan, A. Zettl and Y. M. Wang, Science, 2015, **348**, 1230–1234.

3 K. D. Gilroy, A. Ruditskiy, H. C. Peng, D. Qin and Y. Xia, Chem. Rev., 2016, **116**, 10414–10472.

4 S. Guo, X. Zhang, W. Zhu, K. He, D. Su, A. Mendoza-Garcia, S. F. Ho, G. Lu and S. Sun, J. Am. Chem. Soc., 2014, **136**, 15026–15033.

5 V. M. Dhavale and S. Kurungot, ACS Catal., 2015, **5**, 1445–1452.

6 V. R. Stamenkovic, B. Fowler, B. S. Mun, G. Wang, P. N. Ross, C. A. Lucas and N. M. Marković, Science, 2007, **315**, 493–497.

7 Y. Li, M. Gong, Y. Liang, J. Feng, J. E. Kim, H. Wang, G. Hong, B. Zhang and H. Dai, Nat. Commun., 2013, **4**, 1805.

8 H. Zhang, M. Jin and Y. Xia, Chem. Soc. Rev., 2012, **41**, 8035–8049.

9 M.-H. Shao, K. Sasaki and R. R. Adzic, J. Am. Chem. Soc., 2006, **128**, 3526–3527.

10 Y. Suo, L. Zhuang and J. Lu, Angew. Chem., Int. Ed., 2007, **46**, 2862–2864.

11 R. Choi, J. Jung, G. Kim, K. Song, Y.-I. Kim, S. C. Jung, Y.-K. Han, H. Song and Y.-M. Kang, Energy Environ. Sci., 2014, **7**, 1362–1368.

12 S. Liu, Q. Zhang, Y. Li, M. Han, L. Gu, C. Nan, J. Bao and Z. Dai, J. Am. Chem. Soc., 2015, **137**, 2820–2823.

13 M. Shao, P. Liu, J. Zhang and R. Adzic, J. Phys. Chem. B, 2007, **111**, 6772–6775.

14 M. Shao, T. Huang, P. Liu, J. Zhang, K. Sasaki, M. Vukmirovic and R. Adzic, Langmuir, 2006, **22**, 10409–10415.

15 C. Wang, D. P. Chen, X. Sang, R. R. Unocic and S. E. Skrabalak, ACS Nano, 2016, **10**, 6345–6353.

16 J. Kim, C. Rong, Y. Lee, J. P. Liu and S. Sun, Chem. Mater., 2008, **20**, 7242–7245.

17 M. J. Bierman and S. Jin, Energy Environ. Sci., 2009, **2**, 1050–1059.

18 L. E. Howard, H. L. Nguyen, S. R. Giblin, B. K. Tanner, I. Terry, A. K. Hughes and J. S. Evans, J. Am. Chem. Soc., 2005, **127**, 10140–10141.

19 L. Guo, W.-J. Jiang, Y. Zhang, J.-S. Hu, Z.-D. Wei and L.-J. Wan, ACS Catal., 2015, **5**, 2903–2909.

20 D. Y. Chung, S. W. Jun, G. Yoon, S. G. Kwon, D. Y. Shin, P. Seo, J. M. Yoo, H. Shin, Y. H. Chung, H. Kim, B. S. Mun, K. S. Lee, N. S. Lee, S. J. Yoo, D. H. Lim, K. Kang, Y. E. Sung and T. Hyeon, J. Am. Chem. Soc., 2015, **137**, 15478–15485.

21 Q. Li, L. Wu, G. Wu, D. Su, H. Lv, S. Zhang, W. Zhu, A. Casimir, H. Zhu, A. Mendoza-Garcia and S. Sun, Nano Lett., 2015, **15**, 2468–2473.

22 Y. J. Kim, J. K. Choi, D.-G. Lee, K. Baek, S. H. Oh and I. S. Lee, ACS Nano, 2015, **9**, 10719–10728.

23 N. Cheng, M. N. Banis, J. Liu, A. Riese, X. Li, R. Li, S. Ye, S. Knights and X. Sun, Adv. Mater., 2015, **27**, 277–281.

24 J. Kim, Y. Lee and S. Sun, J. Am. Chem. Soc., 2010, **132**, 4996–4997.

25 D. C. Lee, F. V. Mikulec, J. M. Pelaez, B. Koo and B. A. Korgel, J. Phys. Chem. B, 2006, **110**, 11160–11166.

26 C. Baldizzone, S. Mezzavilla, H. W. Carvalho, J. C. Meier, A. K. Schuppert, M. Heggen, C. Galeano, J. D. Grunwaldt, F. Schüth and K. J. Mayrhofer, Angew. Chem., Int. Ed., 2014, **53**, 14250–14254.

27 C. Galeano, J. C. Meier, V. Peinecke, H. Bongard, I. Katsounaros, A. A. Topalov, A. Lu, K. J. Mayrhofer and F. Schuth, J. Am. Chem. Soc., 2012, **134**, 20457–20465.

28 D. Wang, H. L. Xin, R. Hovden, H. Wang, Y. Yu, D. A. Muller, F. J. DiSalvo and H. D. Abruna, Nat. Mater., 2013, **12**, 81–87.

29 S. Shen, T. Zhao, J. Xu and Y. Li, J. Power Sources, 2010, **195**, 1001–1006.

30 B. Hammer, L. B. Hansen and J. K. Nørskov, Phys. Rev. B: Condens. Matter Mater. Phys., 1999, **59**, 7413–7421.

31 M. Mavrikakis, B. Hammer and J. K. Norskov, Phys. Rev. Lett., 1998, **81**, 2819–2822.